Nanostructures and defects in thermoelectric $AgPb_{18}SbTe_{20}$ single crystal

Lijun Wu,[1,a)] Jin-Cheng Zheng,[1,2] Juan Zhou,[1] Qiang Li,[1] Jihui Yang,[3] and Yimei Zhu[1]
[1]*Brookhaven National Laboratory, Upton, New York 11973, USA*
[2]*Department of Physics and Institute of Theoretical Physics and Astrophysics, Xiamen University, Xiamen 361005, People's Republic of China*
[3]*Materials and Processes Laboratory, General Motors R&D Center, Warren, Michigan 48090, USA*

(Received 19 December 2008; accepted 26 March 2009; published online 6 May 2009)

Nanoparticles play key roles in reducing thermal conductivity, and hence increasing figure of merit for many thermoelectric materials. We have studied the structure of $AgPb_{18}SbTe_{20}$ (LAST-18) using high resolution imaging, nanoelectron diffraction, energy dispersive spectrum, and electron energy loss spectrum, and observed a range of nanoparticles with different sizes (from less than 1 nm to more than 10 nm) and shape (sphere, ellipse, square, etc.). The lattice parameters of the nanoparticles have a wide range from 0.601 to 0.655 nm, while those of the matrix have a range from 0.633 to 0.646 nm. The nanoparticles are formed due to the ordering of Pb and Ag–Sb. There are four ordered structures with primitive cubic, primitive tetragonal (T1, $a \approx a_0/\sqrt{2}$, $c \approx a_0$, here, a_0 is the lattice parameter of the rocksalt-type matrix), primitive tetragonal (T2, $a \approx a_0/\sqrt{2}$, $c \approx 2a_0$), and body-centered tetragonal (T3, $a \approx a_0/\sqrt{2}$, $c \approx 3a_0$) lattices, respectively. Antiphase domains, twins, and phase separations were often observed in the nanoparticles. The strain field in the surrounding matrix due to the presence of nanoparticles was retrieved from the high resolution images. The characteristic that the strain field is anisotropic and extends to large area is considered to enhance the scattering of the phonons. The results provide quantitative structure information about nanoparticles, that is essential for the understanding of the origin of the high thermoelectric performance in this class of materials. © *2009 American Institute of Physics*.
[DOI: 10.1063/1.3124364]

I. INTRODUCTION

With the world's increasing demand for energy and the concern for the environmental impact due to the combustion of fossil fuels, thermoelectric materials, which can convert heat, including waste heat generated by motor vehicles, to electricity are becoming increasingly important in material research. A practical thermoelectric material for the application should have high figure of merit ZT, a parameter determining the efficiency of thermoelectric conversion and is defined as $ZT = \alpha^2 \sigma T/\kappa$, where α, σ, T, and κ are the Seebeck coefficient, electrical conductivity, temperature, and thermal conductivity, respectively.[1] High ZT value is usually obtained by increasing the power factor $\alpha^2\sigma$ and/or decreasing the thermal conductivity κ.[2] Two research approaches are used worldwide for synthesizing promising thermoelectric materials with desirable high ZT value: one using low-dimensional layered structure materials that can scatter electrons and phonons differently,[3] the other using bulk materials with significant amount of defects that are more effective in scattering of phonon than electrons.[4] For the later, a quaternary thermoelectric compound $AgPb_mSbTe_{m+2}$, denoted as LAST-m, has recently attracted great attention due to its high figure of merit (~2.1 at 800 K) that outperforms the other bulk thermoelectric materials.[5] The enhanced thermoelectric properties of LAST-m were attributed to the presence of Ag–Sb-rich nanoparticles which are coherently embedded in the matrix.[5] *Ab initio* electronic calculations based on different Ag–Sb arrangements show that the electronic structure and consequently the electronic and thermal properties of LAST-m system are different from those of PbTe and are very sensitive to the atomistic arrangements of Ag–Sb atoms.[6] Transport studies showed that the enhanced ZT of LAST-m compared to the PbTe is mostly due to a strong reduction in the lattice thermal conductivity due to the presence of the nanoparticles.[7]

The LAST-m compounds possess an average NaCl structure (space group: Fm-3m) with Ag, Sb, and Pb randomly occupying at Na site and Te at Cl site. However, recent studies using x-ray diffraction and high resolution transmission electron microscopy (HRTEM) reveal that LAST-m is inhomogeneous at the nanoscale with at least two coexisting sets of well-defined phases.[8] The nanoparticles with cubic and orthorhombic lattices were found to be Ag–Sb rich and endotaxially embedded in the majority phase which has NaCl structure and is poor in Ag and Sb.[8] A variety of other thermoelectric materials have also been fabricated with similar features of embedded nanoparticles in crystalline semiconductors.[9,10] It is generally believed that nanoparticles in these materials play a key role in reducing thermal conductivity, and therefore enhancing ZT. However, information about the nanoparticles, e.g., atomic arrangements of Pb and Ag–Sb, defects inside the nanoparticle, and strain field induced by the nanoparticles, are still lacking. In this paper, we report our extensive studies about nanoparticles using quantitative HRTEM techniques. The quantitative structure information obtained in LAST-18 can be helpful for the fundamental understanding of this class of materials, by providing

[a)]Electronic mail: ljwu@bnl.gov.

 © 2009 American Institute of Physics

Author complimentary copy. Redistribution subject to AIP license or copyright, see http://jap.aip.org/jap/copyright.jsp

the basis for more realistic theoretical modeling, as well as some guidance for the thermoelectric material design and engineering.

II. EXPERIMENTAL SECTION

A. Synthesis

The single crystalline LAST-18 samples were made by mixing stoichiometric amounts of high purity Pb, Te, Sb, and Ag pieces into a carbon-coated quartz tube. The tube was sealed under vacuum, slowly heated to 1000 °C, and then stayed for 20 h to ensure homogeneity. Subsequently, the tube was cooled to room temperature by turning the power off. The resulting sample was then solidified vertically by the Bridgman method inside a four-zone furnace. It was heated up above 950 °C (about 40 °C above the liquidus) for 3 h, soaked above the liquidus of 910 °C for 61 h as the furnace slowly translated upward at a rate of 0.5 mm/h. When the crystal started to grow, the furnace translation rate was increased to 1 mm/h. After a total translation of 25.5 mm, the translation stopped and the furnace was cooled down by turning the power off.

Electron transparent samples were prepared by conventional mechanical polishing and argon ion milling at about −100 °C to a thickness of around 10–100 nm.

B. HRTEM

HRTEM was performed using JEM-3000F and JEM-2200MCO transmission electron microscopes at Brookhaven National Laboratory. The former is equipped with an ultra-high resolution objective-lens pole piece, an off-axis 1024 × 1024 Gatan slow-scan camera, a Fischione annular dark-field detector, a postcolumn Gatan imaging filter, and a NORAN x-ray detector. The later has an in-column omega filter and two aberration correctors, which is mainly used to observe the extremely small nanoparticles. The magnification and camera length of the microscopes were calibrated using Si and $SrTiO_3$ single crystals. The composition of the nanoparticles was measured by both energy dispersive x-ray spectroscopy (EDS) and electron energy loss spectroscopy (EELS) in the microscopes. Although both EDS and EELS can measure sample composition with reasonable accuracy, we consider the composition measurements of the nanoparticles to be semiquantitative due to the small size of the nanoparticles.

To assist interpretation of the HRTEM images, image simulations were carried out using our own simulation codes based on the multislice method.[11] The distribution of the strain field was retrieved using geometric phase analysis (GPA) from HRTEM images.[12,13] GPA is an image processing technique based on centering a small aperture around a strong reflection (g) in the Fourier transform of a HRTEM image, followed by an inverse Fourier transform. The phase component $P'_g(\boldsymbol{r})$ of the resulting complex image is related to the lattice displacement $\boldsymbol{u}(\boldsymbol{r})$:

$$P_g(\boldsymbol{r}) = P'_g(\boldsymbol{r}) - 2\pi \boldsymbol{g}\cdot\boldsymbol{r} = -2\pi \boldsymbol{g}\cdot\boldsymbol{u}(\boldsymbol{r}), \quad (1)$$

where $\boldsymbol{g}$ is the reciprocal lattice vector describing the undistorted lattice and can be obtained from an undistorted reference area. The two-dimensional displacement field can be derived by applying the method to two noncolinear Fourier components, e.g., $\boldsymbol{g}_1$ and $\boldsymbol{g}_2$,

$$P_{g1}(\boldsymbol{r}) = -2\pi \boldsymbol{g}_1\cdot\boldsymbol{u}(\boldsymbol{r}) = -2\pi\{g_{1x}u_x(\boldsymbol{r}) + g_{1y}u_y(\boldsymbol{r})\}, \quad (2)$$

$$P_{g2}(\boldsymbol{r}) = -2\pi \boldsymbol{g}_2\cdot\boldsymbol{u}(\boldsymbol{r}) = -2\pi\{g_{2x}u_x(\boldsymbol{r}) + g_{2y}u_y(\boldsymbol{r})\}, \quad (3)$$

where g_{1x}, g_{1y}, g_{2x}, and g_{2y} are the x and y components of the $\boldsymbol{g}_1$ and $\boldsymbol{g}_2$ vectors, respectively. $u_x(\boldsymbol{r})$ and $u_y(\boldsymbol{r})$ are the x and y components of the displacement field $\boldsymbol{u}(\boldsymbol{r})$ at the position $\boldsymbol{r}=(x,y)$ in the image. The strain field is then calculated,

$$\varepsilon_{xx} = \frac{\partial u_x}{\partial x}, \quad \varepsilon_{yy} = \frac{\partial u_y}{\partial y}. \quad (4)$$

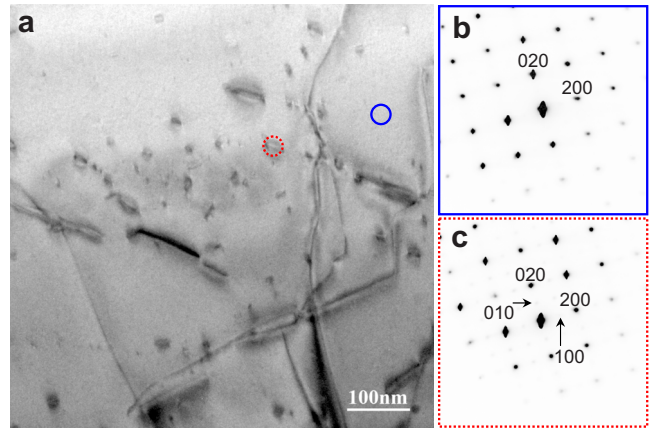

FIG. 1. (Color online) (a) Typical region in a LAST-18 single crystal sample, showing nanoparticles and dislocations. [(b) and (c)] Nanodiffraction patterns taken from (a). (b) Matrix (marked by blue solid circle) is determined to be face-centered cubic which obeys $h+k$=odd extinction rule, and (c) nanoparticle (marked by red dashed circle) which has a primitive lattice with weak spots of 100, 010, etc.

III. RESULTS

An overall observation indicates that dislocations and nanoparticles coherently embedded in the matrix are main structure defects in the sample, as shown in Fig. 1(a). Electron diffraction analysis including tilting the sample to several low-order zones confirms that the matrix has a rocksalt-type structure (space group: Fm-$3m$). The lattice parameter of the matrix varies locally from 0.633 to 0.646 nm, which is caused by the small variation in the composition. Figure 1(b) is the [001] nanoelectron diffraction (NED) pattern by forming a small probe (about 10 nm) on a perfect region of the matrix [marked by blue solid circle in Fig. 1(a)]. The reflections with $h+k$=odd are invisible due to the extinction of the face-centered lattice. Figure 1(c) is the NED from a nanoparticle marked by a red dashed circle in Fig. 1(a) with visible reflections of $h+k$=odd, indicating that the structure of the nanoparticle is different from that of the matrix, and it can be indexed as a primitive cubic lattice as reported by Quarez *et al.*[8] Extensive observations over the samples using high resolution imaging reveal that there are several kinds of nanoparticles in the system with different sizes, shapes, and structures.

Author complimentary copy. Redistribution subject to AIP license or copyright, see http://jap.aip.org/jap/copyright.jsp

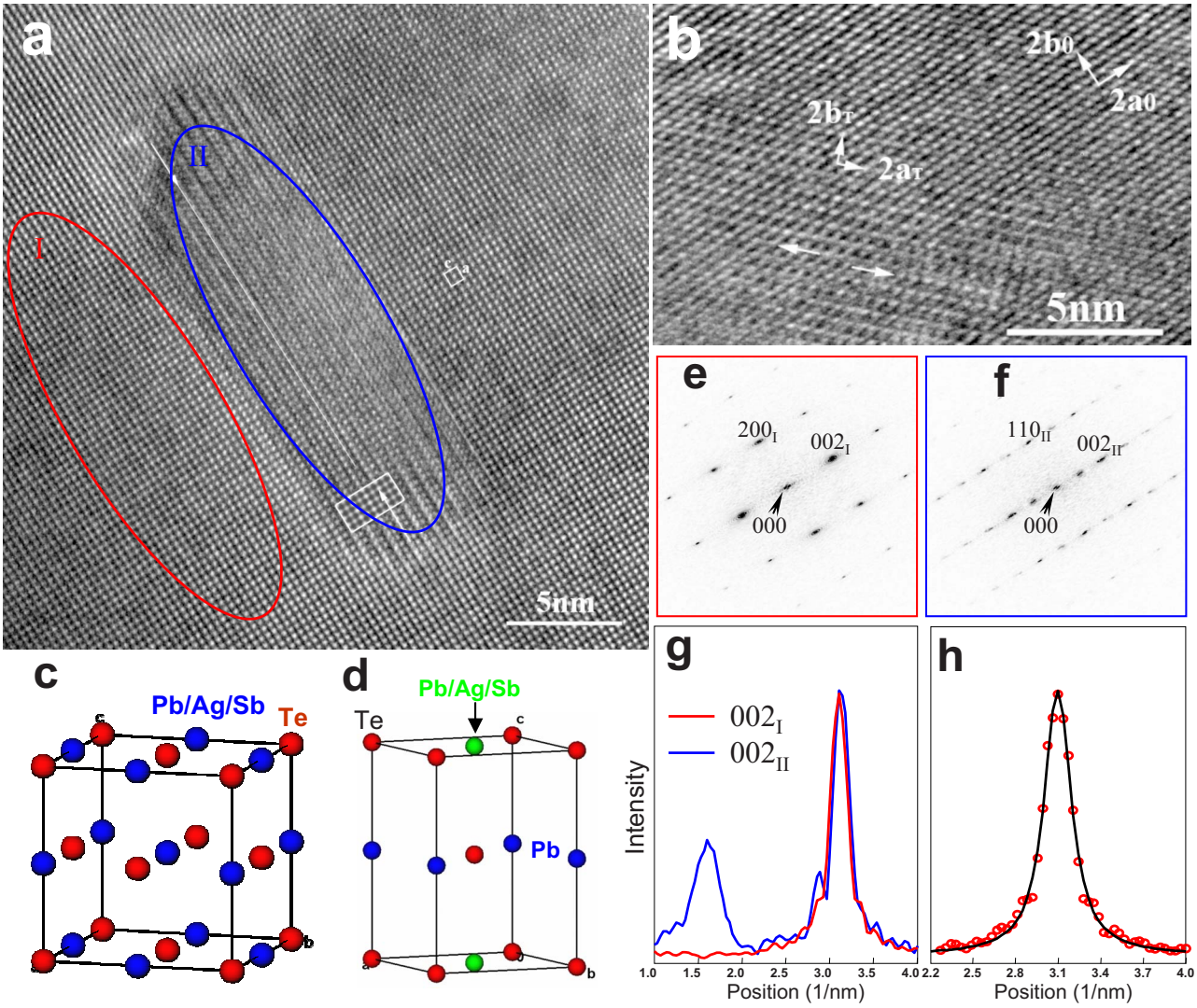

FIG. 2. (Color online) (a) A [010] HRTEM image of LAST-18 single crystal sample, showing a nanoparticle coherently embedded in the matrix. (b) HRTEM image from another area, showing [001] projection of the nanoparticle. The antiphase domains are observed in both images as indicated by the arrows. [(c) and (d)] Atomic models of the matrix (c) and the nanoparticle (d). A calculated HRTEM image is also included [rectangular region in (a)]. [(e) and (f)] Diffractograms from the ellipse areas I (e) and II (f) in (a). (g) 002 intensity profiles from the diffractograms in (e) and (f). The 002 peak in the blue line [from nanoparticle diffractogram (f)] is slightly shifted to the right, indicating that the *c* lattice parameter of the nanoparticle is slightly smaller that that of the matrix. (h) Combined Gaussian and Lorentz fit (black line) to 002 reflection of the matrix (open circles).

A. Structures of nanoparticles

Figure 2(a) is a high resolution image viewed along the [010] direction, showing an elliptical-like nanoparticle coherently embedded in the matrix. In comparison with the unit cell of the matrix, as marked by a square, the unit cell of the nanoparticles clearly shows an ordering along the [001] direction. Moreover, the contrast in the top-left part reverses or shifts one atomic layer along the [001] direction with respect to the bottom-right part of the nanoparticle as marked by the arrows, revealing the existence of antiphase domains. Figure 2(b) is a HRTEM image from another area, showing the [001] projection of the nanoparticle. The structure of the nanoparticle is determined to be primitive tetragonal (here, we denoted it as T1) with $a_{T1} \approx a_0/\sqrt{2}$ and $c_{T1} \approx a_0$ (a_{T1} and c_{T1}, and a_0 are the lattice parameters of the nanoparticle T1 and the matrix, respectively). The primitive tetragonal structure we observed is consistent with x-ray diffraction.[8] Figures 2(c) and 2(d) show the structure models of the matrix and T1, respectively. Comparing to the structure of the matrix which has face-centered cubic lattice, Pb and Pb/Ag/Sb order along *c* direction in the T1 nanoparticle. Apparently, the exchange of Pb and Pb/Ag/Sb, or equivalently $\frac{1}{2}$ [111] shifting of the unit cell yields an antiphase domain.

The composition measurements using both EDS and EELS show that the T1 is slightly Ag–Sb rich. The HRTEM simulation embedded in Fig. 2(a) (the rectangular area), based on the structure model with Pb:Ag:Sb=50:25:25 at Pb/Ag/Sb site [Fig. 2(d)], shows good agreement with the experiment.

To accurately measure the difference of local lattice parameters, e.g., the red ellipse area in Fig. 2(a), we retain the data of an area of interest, while replace the data of the remaining area with a constant value that is the mean value of that area, and Fourier transform the modified image to get the diffractogram of the area of interest, as shown in Fig. 2(e). A intensity profile from the central spot to the reflection

Author complimentary copy. Redistribution subject to AIP license or copyright, see http://jap.aip.org/jap/copyright.jsp

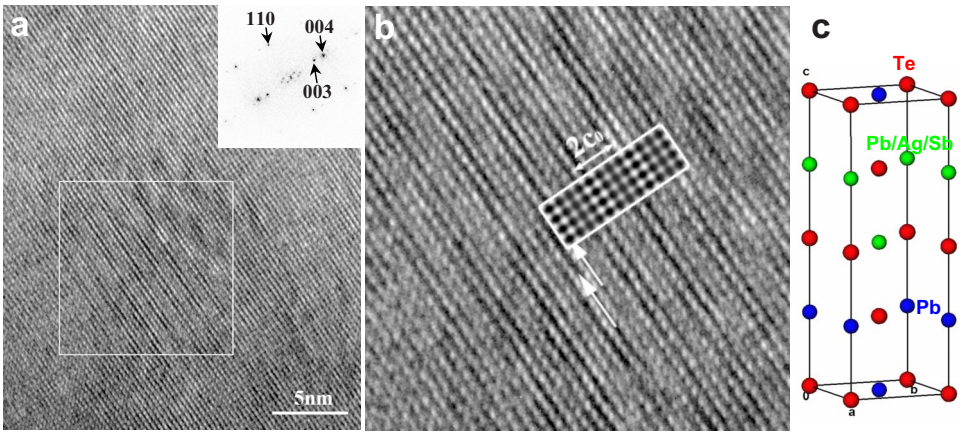

FIG. 3. (Color online) (a) HRTEM image of a nanoparticle with $c \approx 2a_0$. The inset is the diffractogram of the nanoparticle. (b) Magnified image from the marked area in (a). Antiphase domain due to the shift of the unit cell is indicated by the arrows. The simulation is inserted in the middle of the image based on the structure model (c) with the atomic ratio of Pb:Ag:Sb in Pb/Ag/Sb site being 50:25:25 in (c). (c) Structure model of the nanoparticle.

spot is then obtained for the measurement and the comparison of the positions of the reflection spots from the different areas. The red and blue lines in Fig. 2(g) are the 002 profiles from the matrix [Fig. 2(e)] and the nanoparticle [Fig. 2(f)], respectively. It is seen that the 002 peak from the nanoparticle slightly shifts to the right, implying that the lattice parameter c of the nanoparticle is slightly smaller than that of the matrix. The accurate lattice parameter can be obtained by fitting the profile using combination of a Gaussian and a Lorentzian function,

$$I = a_0 \exp\left\{-\left[\frac{x-a_1}{a_2/(2\ln 2)}\right]^2\right\} + \frac{a_3}{4(x-a_1)^2 + a_2^2} + a_4, \quad (5)$$

where a_0 and a_3 are the amplitudes of the Gaussian and Lorentzian functions, respectively, a_1 is the position of the peak, a_2 is the full width of the peak at half maximum height, and a_4 is the base line offset. Here, we use Levenberg–Marquardt method to refine the above parameters.[14] The standard errors in the fitted parameters are estimated by covariance matrix. Figure 2(h) shows the fitting of the 002 matrix peak. The refined position of the 002 matrix peak is $p_{002} = 3.096 \pm 0.011\ \mathrm{nm}^{-1}$. The lattice parameter of the matrix is therefore determined to be $c_0 = 2/p_{002} = 0.646 \pm 0.002$ nm. By fitting the 002 peak of the nanoparticle, the lattice parameter c of the nanoparticle is determined to be 0.640 ± 0.003 nm. The lattice parameters a for the matrix and nanoparticle are determined to be 0.643 ± 0.003 and 0.453 ± 0.002 nm (note that $\sqrt{2} \times a_{T1} = 0.641$), respectively. Comparing to the matrix, the lattice change of the nanoparticle mainly occurs along the [001] direction which is the ordering direction of the nanoparticle and the short axis of the elliptical shape nanoparticle as well.

Figure 3(a) is another HRTEM image from the single crystal sample. Figure 3(b) is the magnified image from the marked area in Fig. 3(a). The periodicity of the nanoparticle along the [001] direction is doubled which is similar to that observed by Quarez *et al.*[8] We denote this kind of nanoparticle as T2. The diffractogram (see inset) from the marked area also shows a superlattice as indicated by the arrow. We noted that the superlattice spots deviate from the g_{002} direction which can be attributed to the antiphase domains as indicated by the arrows in Fig. 3(b). A structure model with primitive tetragonal lattice ($a_{T2} \approx a_0/\sqrt{2}$ and $c_{T2} \approx 2a_0$) is then derived [Fig. 3(c)], in which two PbTe layers are separated by two (PbAgSb)Te layers along c direction. A simulated HRTEM image based on this structure model with Pb:Ag:Sb=50:25:25 at Pb/Ag/Sb site is embedded in Fig. 3(b), showing good agreement with the experiment. The lattice parameters of T2 are refined to be $a_{T2} = 0.453 \pm 0.002$ nm and $c_{T2} = 1.288 \pm 0.004$ nm. The antiphase domains can be attributed to the exchange of Pb and Pb/Ag/Sb, or equivalently the $\left[\frac{1}{2}\frac{1}{2}\frac{1}{4}\right]$ shift of the unit cell in one domain with respect to the neighbor domain.

Figure 4(a) shows a nanoparticle with its periodicity

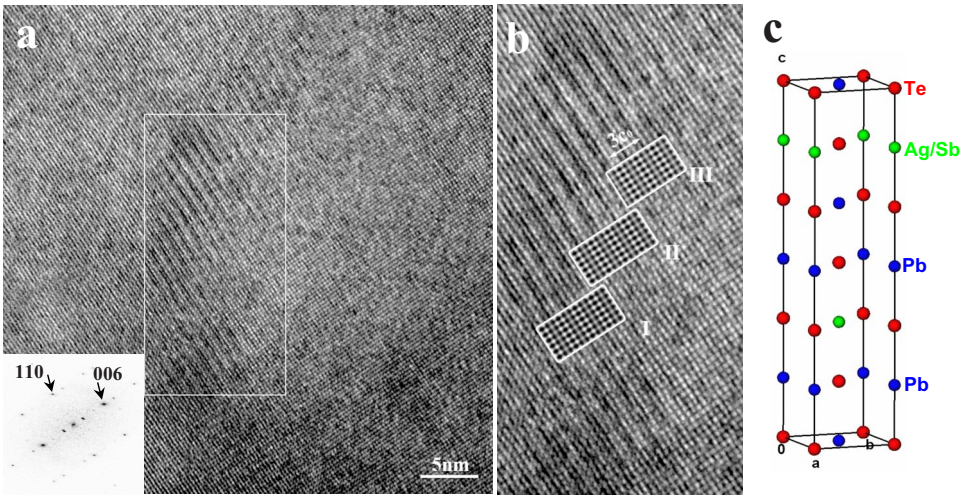

FIG. 4. (Color online) (a) HRTEM image of a nanoparticle with $c \approx 3a_0$. The inset is the diffractogram of the nanoparticle. (b) Magnified image from the marked area in (a). The embedded images are simulations based on the structure model shown in (c). Areas II and III are the same as inset I but is shifted one and two atomic layers along the [001] direction with respect to I, respectively. (c) Structure model of the nanoparticle.

Author complimentary copy. Redistribution subject to AIP license or copyright, see http://jap.aip.org/jap/copyright.jsp

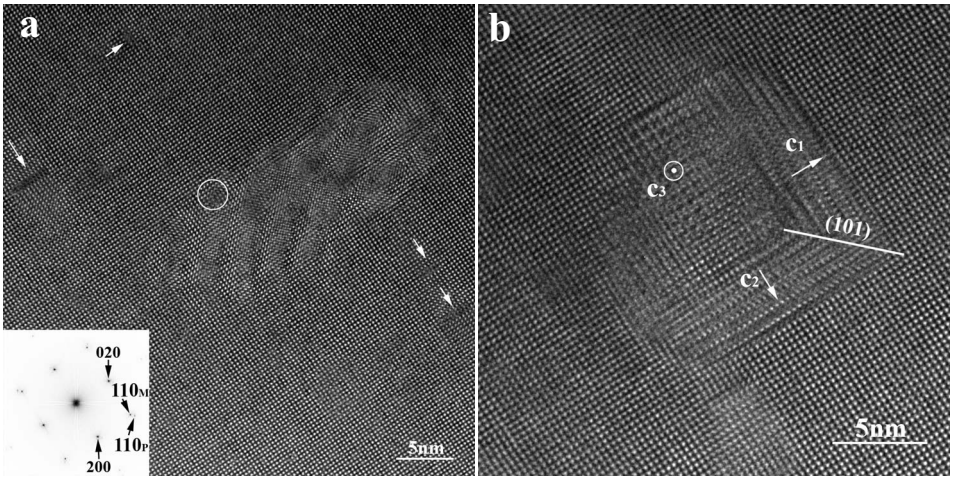

FIG. 5. (a) HRTEM image of $AgSbTe_2$ nanoparticle in PbTe matrix. The inset is the diffractogram of the whole image, showing that the reflections of the matrix and nanoparticle are well separated. Morié pattern due to the overlap of the nanoparticle and the matrix in the projection is also visible. Interfacial dislocations and platelike nanoprecipitates with two atomic layer thicknesses are also present as indicated by the circle and arrows, respectively. (b) Twinning in square shape nanoparticle.

along the c direction tripled. We denoted this newly found nanoparticle as T3. Figure 4(b) is the magnified image from the marked area. The shape of the T3 is irregular. There is no sharp boundary between the matrix and T3. Antiphase domains also present. A body-center tetragonal structure model with $a_{T3} \approx a_0/\sqrt{2}$ and $c_{T3} \approx 3a_0$ is shown in Fig. 4(c). The lattice parameters of T3 are refined to be $a_{T3} = 0.448 \pm 0.002$ nm and $c_{T3} = 1.917 \pm 0.005$ nm. Three boxed images in Fig. 4(b) are simulated HRTEM images based on the structure model with the arrangements of PbTe/(AgSb)Te/PbTe/PbTe/(AgSbTe)/PbTe along c direction [Fig. 4(c)]. The area II shifts 0.3195 nm (one atomic layer) along the [001] direction with respect to the area I, and area III shifts additional 0.3195 nm. Apparently, the antiphase domains are due to the $\left[\frac{1}{2}\frac{1}{2}\frac{1}{6}\right]$ shift of the unit cell in one domain with respect to the adjacent domains.

All nanoparticles we showed above have a coherent interface with respect to the matrix. The corresponding lattice mismatch between the nanoparticles and the surrounding matrix is less than 1%. No interfacial dislocations were observed. Figure 5(a) is an energy filtered HRTEM image obtained from JEM-2200MCO, showing large lattice difference between the nanoparticle and the matrix. The diffractogram from the whole image shows well separate diffraction spots between the nanoparticle and the matrix. EDS measurement shows that the concentration of Ag and Sb in the nanoparticle area is significantly larger than that in the neighboring matrix. The diffractogram taken from the nanoparticle still shows weak matrix spots due to the overlap of the matrix and the nanoparticle along the image projection, so as the Morié pattern (interference pattern produced when two crystals having differences in lattice parameter or orientation overlap). The presence of the interfacial dislocations, marked by the circle in Fig. 5(a), is to accommodate the misfit between the matrix and the nanoparticle. The lattice parameter of the matrix is refined to be $a_0 = 0.646 \pm 0.002$ nm, whereas the lattice parameters of the nanoparticle to be $a = 0.601 \pm 0.003$ nm and $c = 0.608 \pm 0.003$ nm. Based on the relationship between the composition and lattice parameter in the $AgSbTe_2$–PbTe system,[15] it suggests that the nanoparticle be $AgSbTe_2$, while the surrounding matrix be PbTe. Figure 5(b) shows a square-shape nanoparticle with T1 structure. Three twin variants with their $\boldsymbol{c}$ direction pointing to $\boldsymbol{c}_1$, $\boldsymbol{c}_2$, and $\boldsymbol{c}_3$ exist in the nanoparticle, which are expected based on the space group theoretical consideration.[16] The precipitation of the T1 nanoparticle from the matrix results in symmetry reduction from cubic to tetragonal due to the loss of fourfold symmetry along $\boldsymbol{a}$ and $\boldsymbol{b}$ axes. The T1 phase has an equal probability of being generated with its unique fourfold axis ($\boldsymbol{c}$ axis) along $\boldsymbol{a}$, $\boldsymbol{b}$, or $\boldsymbol{c}$ axis of the parent phase (the matrix) since $\boldsymbol{a}$, $\boldsymbol{b}$, and $\boldsymbol{c}$ are equivalent in the parent phase, thus possess three twin variants.

Careful observations, especially using aberration-corrected TEM, reveal that there are also tiny platelike nanoprecipitates, as indicated by the arrows in Fig. 5(a). Their dimension is only 0.644 nm (2 atomic layers) in one dimension and varies from 1.22 nm (4 atomic layers) to 3.86 nm (12 atomic layers) in the other two dimensions. The atomic structure of the tiny platelike nanoprecipitates has been derived using density functional theory (DFT) calculations with a large supercell containing 1728 atoms.[17]

B. Strain field associated with the nanoparticles

Strain contrast around the nanoparticles is observed for most of the nanoparticles. An example is given in Figs. 6(a) and 6(b). The diffractograms of the nanoparticle (area I) and the matrix (area II) are shown in Figs. 6(c) and 6(d), respectively. The weak 001 and 100 spots in the diffractogram of the nanoparticle [Fig. 6(c)] indicate that the nanoparticle has a primitive lattice. The intensity profiles (black, red, and blue) from the 002 peaks of the diffractograms of area I [Fig. 6(c)], II [Fig. 6(d)], and III are shown in Fig. 6(e). The black profile from the diffractogram of the nanoparticle shows the split of the 002 peaks. One is at 3.064 ± 0.023 nm^{-1}, the other is at 3.255 ± 0.021 nm^{-1} positions. This implies that the nanoparticle consists of two phases, one with the lattice parameter $c_{I1} = 0.653 \pm 0.005$ nm, while the other with $c_{I2} = 0.614 \pm 0.003$ nm. The 200 intensity profile [black line in Fig. 6(f)] of the nanoparticle is quite broad with an average value of $a_I = 0.617$ nm. The lattice parameter of the matrix in area II, refined from the red line, is determined to be $c_{II} = 0.638 \pm 0.002$ nm, while that in area III (blue) to be $c_{III} = 0.633 \pm 0.002$ nm, about 0.8% smaller than that at area II. The lattice parameters along the [100] direction are refined to be $a_{II} = 0.632 \pm 0.002$ nm and $a_{III} = 0.634 \pm 0.002$ nm for the

Author complimentary copy. Redistribution subject to AIP license or copyright, see http://jap.aip.org/jap/copyright.jsp

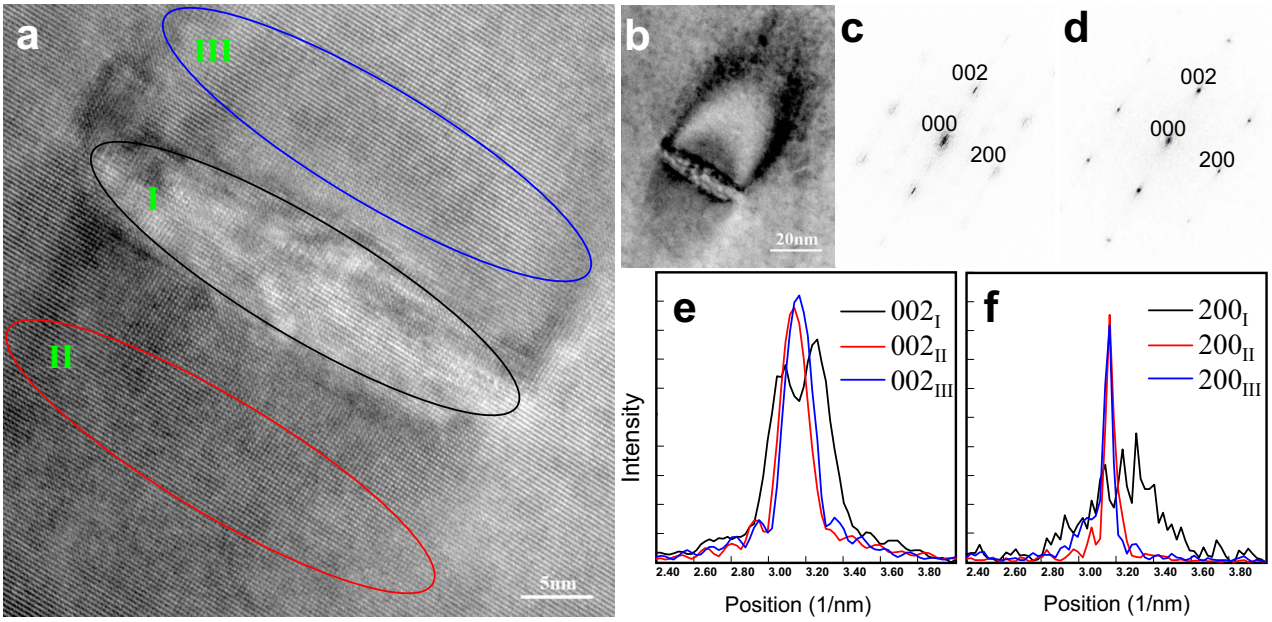

FIG. 6. (Color online) (a) HRTEM image of an elliptical nanoparticle. (b) Low-magnification image of (a), showing strain field contrast. [(c) and (d)] Diffractograms from the elliptical area I (c) and II (d). (e) 002 intensity profiles from (c), (d) and the diffractogram of area III (not shown). (f) 200 intensity profiles from (c), (d) and the diffractogram of area III.

matrix at areas II and III, respectively. The difference is within the measurement error. Comparing to the average lattice parameter of the matrix (0.644 nm), e.g., far away from the nanoparticle, the lattice parameter of the matrix here is about 1.6% smaller, indicating a compressed strain field in the surrounding matrix. The strain field is asymmetric along the $\boldsymbol{c}$ direction which is the short axis of the ellipselike nanoparticle.

The distribution of the strain field can be retrieved using the GPA software. We note that the strain map derived by GPA software is a relative strain map with respect to the reference area. In the case that there is no undistorted area in the image, we first choose a rectangle area as a reference to retrieve a relative strain map, measure the averaged lattice parameter in this reference area to calculate its averaged strain, and then add this averaged strain to the relative strain measurement to get an actual strain field map. Figures 7(a) and 7(b) show the actual strain map ε_{xx} and ε_{yy}, retrieved from the HRTEM image in Fig. 6(a) with $\boldsymbol{g}_1=200$ and $\boldsymbol{g}_2=002$, and x- and y-axes pointing to the [100] and [001] directions. The reference area marked by a yellow rectangle in Fig. 7(b) was measured to have an average strain value of −0.016 in both directions with respect to the undistorted area. The ε_{xx} map basically shows negative strain in both matrix and nanoparticle with large negative amplitude in the nanoparticle. The ε_{yy} map shows positive and negative strains in the nanoparticle area, indicating a phase separation in this nanoparticle, consistent with the lattice measurement using diffractogram. The strain in the matrix, however, is quite different from that generated by an isotropic misfitting spherical inclusion in an infinite isotropic matrix. First, the strain amplitude does not decrease with the increase in the distance from the nanoparticle at least in the range of the measurement (~20 nm). The low magnification bright-field image [Fig. 6(b)] shows that the strain contrast extends to the area about 55 nm away from the nanoparticle (approximately six times the physical size of the nanoparticles), where there still exists about 0.2% strain. Second, the ε_{yy} strain around nanoparticle is not symmetric, although the shape of the nanoparticle looks like a symmetric ellipse. The value of ε_{yy} at bottom left is larger than that at top right. Near the nanoparticle, there is a small region showing a positive value of ε_{yy}. We therefore consider that the strain field around the nanoparticle is not only caused by the misfit between the nanoparticle and the matrix but also by the local fluctuation in the composition. When nanoparticle precipitates, it consumes the Ag–Sb, resulting in the stoichiometric fluctuation in the surrounding matrix. The unusual strain field caused by composition fluctuation was often observed in the LAST-18 single crystals. The strain field retrieved from Fig. 2(a) also shows an asymmetric strain field with the positive strain at bottom left and negative strain at top right of the nanoparticle.

IV. DISCUSSIONS

Assuming that the phonon scattering processes can be represented by frequency-dependent relaxation times, the lattice thermal conductivity can then be obtained by integrating relaxation times from various processes.[18,19] The combined relaxation time τ_c is given by[19]

$$\tau_c^{-1} = \tau_P^{-1} + \tau_D^{-1} + \tau_B^{-1} + \tau_{\mathrm{EP}}^{-1} + \tau_A^{-1}, \tag{6}$$

where $\tau_P^{-1}=C_P\omega^2$ is the reciprocal relaxation time due to phonon-phonon scattering, including normal and umklapp processes,[18–20] $\tau_D^{-1}=C_D\omega^4$ due to point-defect scattering,[21–23] $\tau_B^{-1}=v_s/L$ due to boundary scattering,[18] τ_{ED} due to phonon-electron scattering,[24,25] and τ_A due to alloying effects. C_P and C_D are coefficients, v_s is the velocity of sound, and L is a characteristic length, e.g., the average diameter of the grains for polycrystalline material.[26] The lattice thermal conductiv-

Author complimentary copy. Redistribution subject to AIP license or copyright, see http://jap.aip.org/jap/copyright.jsp

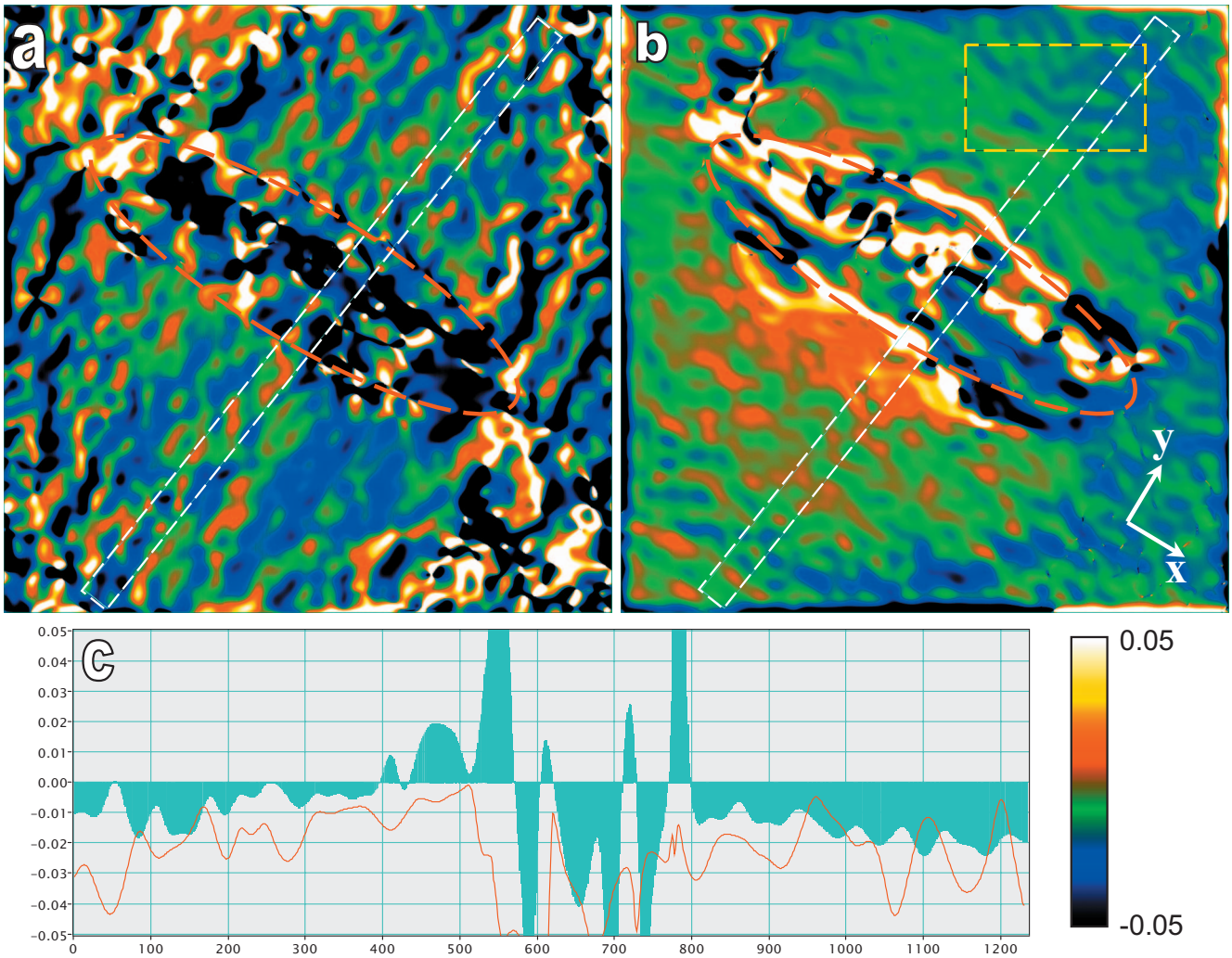

FIG. 7. (Color) Strain map of (a) ε_{xx} and (b) ε_{yy} calculated from the HRTEM image shown in Fig. 6(a). The yellow rectangle in (b) is the reference area which has an averaged strain of −0.016. The maps are shown in color for clarity. The ellipses in the figures outline the nanoparticles. (c) Profiles of the strain, red line from (a), and green line from (b).

ity can then be calculated using the Callaway's formalism,[18,19]

$$\kappa = \frac{k_B}{2\pi^2 v_s}\left(\frac{k_B T}{\hbar}\right)^3 \int_0^{\theta_D/T} \tau_c(x)\frac{x^4 e^x}{(e^x-1)^2}dx, \tag{7}$$

where θ_D is the Debye temperature and $x=\hbar\omega/k_B T$ is the dimensionless variable. It is seen that the high-frequency phonons can be significantly cut by the point defects, such as substitutional atoms and vacancies. The mid-to-long-wavelength phonons can be scattered by nanoparticles.[27] Earlier calculations for spherical inclusions of 4 nm diameter in Si–Ge showed that the lattice thermal conductivity can be substantially reduced.[26] Recent experiments by embedding ErAs nanoparticles demonstrated that the lattice thermal conductivity in $In_{0.53}Ga_{0.47}As$ can be reduced by almost a factor of 2 below the alloy limit and the *ZT* can be increased by a factor of 2.[27] In LAST-18, the nanoparticles with a wide size and shape distribution effectively scatter a wide range of spectra of phonons. The platelike nanoparticles which are only two atomic layers thick [see Fig. 5(a)] may scatter short-wavelength phonons as well. The coherent nanocrystals/matrix interfaces may further scatter phonons while have little effect to electrons. We noted that when the size of the nanoparticles is close to, or more than, 10 nm, there exist often antiphase boundaries [Fig. 2(a)], twin boundaries [Fig. 5(a)], and phase separations [Fig. 6(a)] in the nanoparticles, which provide additional boundaries to scatter phonons, thus further reduce thermal conductivity of the compound.

Strain field was considered to reduce thermal conductivity and enhance thermoelectric performance in $(AgSbTe_2)_{1-x}(GeTe)_x$.[28] It has been pointed out by Carruthers[29,30] that with proper consideration of strain field effects, the thermal conductivity can be reduced by three orders of magnitude in lithium fluoride.[31] The thermal resistivity due to the strain is independent of temperature since the distribution of phonons among the various modes does not change with temperature, nor the scattering probability.[30] For a sphere embedded in an isotropic elastic medium, the reciprocal relaxation time can be expressed by[30]

$$\tau^{-1} = 0.25\sigma(gA'/\rho)^2 \times (q^2/c^2), \tag{8}$$

where $A'=\varepsilon r_0^2$ (r_0 is the radius of the sphere and ε is a constant related to the misfit between the sphere and the

Author complimentary copy. Redistribution subject to AIP license or copyright, see http://jap.aip.org/jap/copyright.jsp

matrix). However, the strain around the nanoparticles in LAST-18 generally cannot be simply modeled by above isotropic elastic theory due to the composition fluctuation in the surrounding matrix. The features that the strain field due to the nanoparticles in LAST-18 is anisotropic and extends to large area may have more effect on the phonon scattering, thus likely play a significant role in reducing the lattice thermal conductivity. It has been shown that PbTe is a narrow gap semiconductor. By alloying $AgSbTe_2$, the band structures of LAST-*m* change with the percentage of $AgSbTe_2$ (or value of *m*). Our preliminary DFT calculations show that some ordered phases in LAST-*m* with certain concentration of Ag/Sb become metallic or have narrower band gaps. This suggests that both electron-phonon scattering and electronic contribution in LAST-*m* can be enhanced, and thus provide more competing sources for overall thermal conductivity.

V. CONCLUSIONS

The nanoparticles with different sizes and shapes in LAST-18 have been analyzed in detail using quantitative HRTEM. The nanoparticles are generally Ag–Sb-rich and well oriented within the rocksalt -type matrix with coherent interfaces. The lattice difference between nanoparticles and surrounding matrix varies from less than 1% to 6%. Antiphase domains, twins, and phase separations were often observed when the nanoparticles are large in size. Besides the primitive cubic and primitive tetragonal structures, a new structure with body-centered tetragonal lattice and tripled lattice parameter along ***c*** direction was observed. The strain field in the surrounding matrix due to the presence of nanoparticles shows anisotropic and long range characteristics. The structural features of the nanoparticles we observed in the LAST-18 may very likely exist in other nanocomposite materials with coherent grain boundaries, and hence the quantitative information, as well as the methods to retrieve such information, we reported here may be useful for understanding broad classes of multicomponent nanocomposite materials.

ACKNOWLEDGMENTS

Work at Brookhaven National Laboratory was supported by the U.S. Department of Energy, Office of Basic Energy Science, under Contract No. DE-AC02-98CH10886. Work at GM was supported by GM and DOE under Cooperative Agreement No. DE-FC26-04NT 42278.

[1]H. J. Goldsmid, *Thermoelectric Refrigeration* (Plenum, New York, 1964).
[2]C. M. Bhandari and D. M. Rowe, *CRC Handbook of Thermoelectrics* (CRC, Boca Raton, FL, 1995), p. 43.
[3]L. D. Hick and M. D. Dresselhaus, Phys. Rev. B **47**, 12727 (1993); **47**, 16631 (1993).
[4]B. D. Sales, D. Mandrus, and R. K. Williams, Science **272**, 1325 (1996).
[5]K. F. Hsu, S. Loo, F. Guo, W. Chen, J. S. Dyck, C. Uher, T. Hogan, E. K. Polychroniadis, and M. G. Kanatzids, Science **303**, 818 (2004).
[6]D. Bilc, S. D. Mahanti, E. Quarez, K. F. Hsu, R. Pcionek, and M. G. Kanatzidis, Phys. Rev. Lett. **93**, 146403 (2004).
[7]D. Bilc, S. D. Mahanti, and M. G. Kanatzidis, Phys. Rev. B **74**, 125202 (2006).
[8]E. Quarez, K.-F. Hsu, R. Pcionek, N. Frangis, E. K. Polychroniadis, and M. G. Kanatzidis, J. Am. Chem. Soc. **127**, 9177 (2005).
[9]P. F. P. Poudeu, J. D'Angelo, H. Kong, A. Downey, J. L. Short, R. Pcionek, T. P. Hogan, C. Uher, and M. G. Kanatzidis, J. Am. Chem. Soc. **128**, 14347 (2006).
[10]P. F. P. Poudeu, Angew. Chem., Int. Ed. **45**, 3835 (2006); W. Kim, J. Zide, A. Gossard, D. Klenov, S. Stemmer, A. Shakouri, and A. Majumdar, Phys. Rev. Lett. **96**, 045901 (2006).
[11]E. J. Kirkland, *Advanced Computing in Electron Microscopy* (Plenum, New York, 1998).
[12]M. J. Hÿtch, E. Snoeck, and R. Kilaas, Ultramicroscopy **74**, 131 (1998).
[13]M. J. Hÿtch, J.-L. Putaux, and J.-M. Pénisson, Nature (London) **423**, 270 (2003).
[14]W. H. Press, S. A. Teukolsky, W. T. Vetterling, and B. P. Flannery, *Numerical Recipes in C* (Press Syndicate of University of Cambridge, Cambridge, 1992), p. 683.
[15]F. D. Rosi, E. F. Hockings, and N. E. Lindenblad, RCA Rev. **22**, 82 (1961).
[16]L. Wu and Y. Zhu, Philos. Mag. A **76**, 481 (1997).
[17]X. Ke, C. Chen, J. Yang, L. Wu, J. Zhou, Q. Li, Y. Zhu, and P. R. Kent (unpublished).
[18]J. Callaway, Phys. Rev. **113**, 1046 (1959).
[19]J. Callaway and H. C. Von Baeyer, Phys. Rev. **120**, 1149 (1960).
[20]P. G. Klemens, Phys. Rev. **119**, 507 (1960).
[21]P. G. Klemens, Proc. Phys. Soc., London, Sect. A **68**, 1113 (1955).
[22]B. Abeles, Phys. Rev. **131**, 1906 (1963).
[23]M. W. Ackerman and P. G. Klemens, J. Appl. Phys. **42**, 968 (1971).
[24]J. M. Ziman, Philos. Mag. **1**, 191 (1956); **2**, 292 (1957).
[25]E. F. Steigmeier and B. Abeles, Phys. Rev. **136**, A1149 (1964).
[26]D. P. White and P. G. Klemens, J. Appl. Phys. **71**, 4258 (1992).
[27]W. Kim, J. Zide, A. Gossard, D. Klenov, S. Stemmer, A. Shakouri, and A. Majumdar, Phys. Rev. Lett. **96**, 045901 (2006).
[28]E. A. Skrabek and D. S. Trimer, *CRC Handbook of Thermoelectrics* (CRC, Boca Raton, FL, 1995), p. 267.
[29]P. Carruthers, Phys. Rev. **114**, 995 (1959).
[30]P. Carruthers, Rev. Mod. Phys. **33**, 92 (1961).
[31]R. Sproull, M. Moss, and H. Weistock, J. Appl. Phys. **30**, 334 (1959).

Author complimentary copy. Redistribution subject to AIP license or copyright, see http://jap.aip.org/jap/copyright.jsp